

Tuning the Electronic States of Bi₂Se₃ Films with Large Spin-Orbit Interaction Using Molecular Heterojunctions

M. Rogers,¹ C. Knox,¹ B. Hickey,¹ L. Ansari,² F. Gity,² T. Moorsom,^{1,3} M. McCauley,⁴ G. Teobaldi,⁵ M. dos Santos Dias,⁵ H. B. Vasili,¹ M. Valvidares,⁶ M. Ali,¹ G. Burnell,¹ A. Yagmur,¹ S. Sasaki¹ and O. Cespedes^{1,†}

1. School of Physics and Astronomy, University of Leeds, Leeds, U.K.

2. Micronano Electronics Group, Tyndall National Institute, University College Cork, Cork, Republic of Ireland

3. School of Chemical and Process Engineering, University of Leeds, Leeds, U.K.

4. SUPA, School of Physics and Astronomy, University of Glasgow, Glasgow, U.K.

5. Scientific Computing Department, Science & Technology Facilities Council UKRI, Rutherford Appleton Laboratory, Didcot OX11 0QX, U.K.

6. ALBA Synchrotron Light Source, 08290 Cerdanyola del Vallès, Barcelona, Catalonia, Spain

[†]Corresponding author email address: o.cespedes@leeds.ac.uk

An electric bias can shift the Fermi level along the Dirac cone of a topological insulator and modify its charge transport, but tuning the electronic states and spin-orbit interaction (SOI) without destroying the surface topology is challenging. Here, we show that thin film Bi₂Se₃/n-p (p-n) molecular diodes form ordered interfaces where charge transfer and orbital re-hybridisation result in a decrease (increase) of the carrier density and improved mobility. In Bi₂Se₃ the spin-orbit lifetime, τ_{so} , is 0.13 ps, which is comparable to the strongest spin-orbit materials. This lifetime drops further to 0.06 ps (0.09 ps) with the addition of p-n (n-p) molecular diodes, at the limit of measurable values. This strengthened spin-orbit interaction occurs even though molecules are made of light elements and increase the mean free path of the charge carriers by almost 50%, indicating changes to the Berry curvature and/or Rashba splitting around the hybridisation points. Raman spectroscopy gives evidence that the coupling effect may be controlled by optical irradiation, opening a pathway towards the design of heavy-light element hybrids with optically tunable quantum transport.

I. Introduction

The tunability of charge transport in Dirac materials such as the Topological Insulator (TI) Bi_2Se_3 is one of their most attractive aspects for applications in conventional electronics. With a dielectric gate it is possible to control the carrier type, concentration and mobility. However, processes to add oxide electrodes may result in damage of the surface states. Furthermore, the influence of the electrical bias is restricted to shifting the Fermi level along the Dirac cone without altering the density of states, so biasing has a limited influence in the quantum transport properties of the material. TIs are materials where, ideally, the bulk of the sample is insulating and the surface states are conducting, topologically protected. The SOI is key to their magneto-electronic properties, such spin-momentum locking and spin dependent electron scattering that can be converted into an electric voltage via spin accumulation and the imbalance in chemical potential for each orientation -the inverse spin Hall effect. The SOI then controls applications such as the photo-galvanic effect, spin transfer torque in magneto-resistive random-access memories (STT-MRAM), [1–4] unidirectional spin Hall effect, [5] weak anti-localisation and polarised dynamics. Some of the issues that prevent the adoption of Dirac materials in technologies include interface and electrical contact problems, with resistivity mismatch resulting in charge accumulation and scattering, interdiffusion and lack of SOI tunability. [6–8]

Molecular materials offer an alternative to conventional bias gating with oxide electrodes by forming hybrid states that allow for spin filtering, spin photovoltaics and efficient spin-voltage conversion. [9] For example, sub-ML coverage of Bi_2Se_3 with Manganese-Phthalocyanine (MnPc) shifts the Dirac point while the topological states remain unaffected. [10] FePc grown on Bi_2Te_3 gives rise to a supermolecular lattice where the magnetic moment of Fe(II) persists with an in-plane magnetic easy axis without destroying the topological surface states. [11] C_{60} overlayers result in the formation of dispersive conduction bands. [12] Growth of F4TCNQ and $\text{Co}(\text{acac})_3$ on Bi_2Se_3 results in a higher stability in atmosphere, with a mobility enhanced and sustained for months in ambient conditions. [13] Furthermore, organic materials, despite being made mostly of carbon and hydrogen, can give rise to strong spin-orbit effects, either due to their intrinsic curvature, via interface Rashba effects, by the inclusion of metal centres, or due to charge transfer and hybridisation. [14–17] In order to enhance and tune these effects, we use molecular bilayers where one of the materials is an n-type molecule with electron carriers and strong electron affinity (C_{60}) and the other is a p-type hole-conductor molecule (Mn phthalocyanine). The use of both molecules in a diode bilayer leads to a built-in bias that, combined with the charge transfer and hybridisation effects at the TI surface, can be used to tune not only the charge transport, but also the spin-orbit interaction and band structure of Bi_2Se_3 . Furthermore, because of the opto-electronic properties of the molecules, light irradiation can be used to tune these effects. The aim is to enhance spin-dependent electronic effects such as the Berry

curvature, itself linked to symmetry-breaking interactions such as those present at the molecular interface. Altering the effective SOI and Berry curvature would enable the tuning of not only charge transport, but also weak antilocalisation, molecular dynamics, spin-torque and spin-voltage conversion effects amongst others.

II. Structural and Interface Characterisation

We grew 14 nm thick Bi_2Se_3 films by molecular beam epitaxy on sapphire substrates, and molecular bilayers are then deposited in-situ without breaking vacuum by thermal evaporation -see Methods for details. The resulting multilayers are highly ordered, with both TI and molecular films showing crystalline order in cross-section transmission electron microscopy (TEM) images and Xray diffraction peaks (Figs. 1a-c). Atomic resolution, aberration corrected TEM images provide evidence for electron transfer at the $\text{Bi}_2\text{Se}_3/\text{C}_{60}$ interface, where local charged points can be observed as brighter molecular regions. The localised charges will act as local scattering points and, due to changes in orbital geometry and hybridisation, the Berry curvature may increase around these points. [18] Energy Filtered Transmission Electron Microscopy (EFTEM) elemental analysis of the structures shows little or no interdiffusion, although high resolution analysis of phthalocyanine layers is challenging due to beam damage even at low voltages/energies (Figs. 1d-e).

Supplementary Figure S1 shows the resistivity as a function of temperature, with the data extrapolated to zero Kelvin to determine ρ_0 , the limit of elastic impurity scattering. The fits of the Bloch-Grüneisen function return the phonon resistivity and the Debye temperature. The overlayers did not change the phonon resistivity, but the Debye temperatures for the overlaid samples were a bit lower. In all samples the elastic mean free path ($l = v_F \tau_0$) is larger than the thickness and hence the samples are two-dimensional with respect to transport, with larger diffusion constants in the case of molecular diode-tuned states.

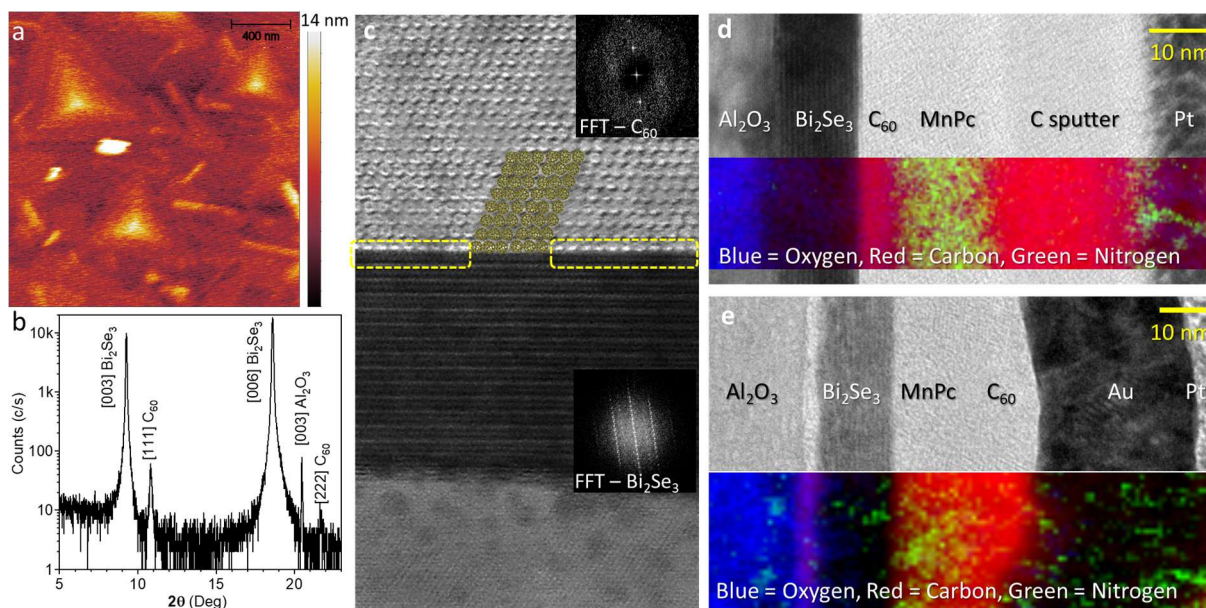


Figure 1| Structural characterisation. **a.** Cross-sectional Transmission Electron Microscope images of show a highly ordered $\text{Bi}_2\text{Se}_3/\text{C}_{60}$ interface with (111) FCC molecular crystal arrangement. **b.** Atomic Force Microscopy shows the triangular Bi_2Se_3 crystals on the surface. **c.** Xray Diffraction with the peaks corresponding to [001] Bi_2Se_3 and [111]. EFTEM sections for **d.** $\text{Bi}_2\text{Se}_3/\text{n-p}$ and **e.** $\text{Bi}_2\text{Se}_3/\text{p-n}$ show well-defined layers with little or no interdiffusion.

III. Molecular Gating of Charge Transport

Similarly to an electric field bias, hybridisation and charge transfer at the molecular interface alter the carrier density and mobility of the system. Carrier density and mobility is determined via Hall effect measurements comparing devices cut from the same TI wafer but where only part is covered with a molecular bilayer. The organic diodes result in changes to the carrier density of Bi_2Se_3 that can be replicated by a top gate bias of ± 10 V across a 24 nm thick Al_2O_3 dielectric layer. However, in the case of the alumina gate, the mobility and spin-orbit lifetime are not enhanced, while the carrier density increase is significantly less than for the molecular gate. Density Functional Theory calculations show changes in the band structure, including the possible emergence of flat bands that are precursor of strange metal behaviour. [19,20]

The acceptor-donor (C_{60} -MnPc) heterojunction generates a dipole dependent on the molecular arrangement. [21–23] Phthalocyanines grow edge-on when deposited on the fullerenes, which results in a charge transfer from C_{60} to MnPc. We can model this heterojunction effect as a p-doped C_{60} layer or with an in-built potential -Fig. 2e. A negative potential or p-doped molecule show a charge accumulation at the $\text{Bi}_2\text{Se}_3/\text{C}_{60}$ interface, in agreement with the increased interface brightness observed in TEM images. Whereas the carrier density of Bi_2Se_3 is reduced by 50% by a C_{60} overlayer, the $\text{C}_{60}/\text{CuPc}$ heterojunction reduces the carrier density just by 26% (Table 1). Fig. 2e illustrates the influence of an external electric field and molecular doping on charge transfer between the C_{60}

molecule and Bi_2Se_3 . This graph represents charge redistribution and net charge transfer as functions of position along the z -direction, perpendicular to the surface. The result highlights how different external factors influence charge redistribution, where the peaks indicate charge accumulation, and the dips correspond to charge depletion. Similar to the charge density, total charge changes are very small far from the $\text{C}_{60}/\text{Bi}_2\text{Se}_3$ interface, indicating minimal charge movement in these regions (Fig. 2e bottom). The extent of charge transfer varies depending on the applied electric field and doping type. These variations reflect the combined effects of polarisation, dipole formation due to the electric field, and charge donation induced by p -type doping of the C_{60} molecule.

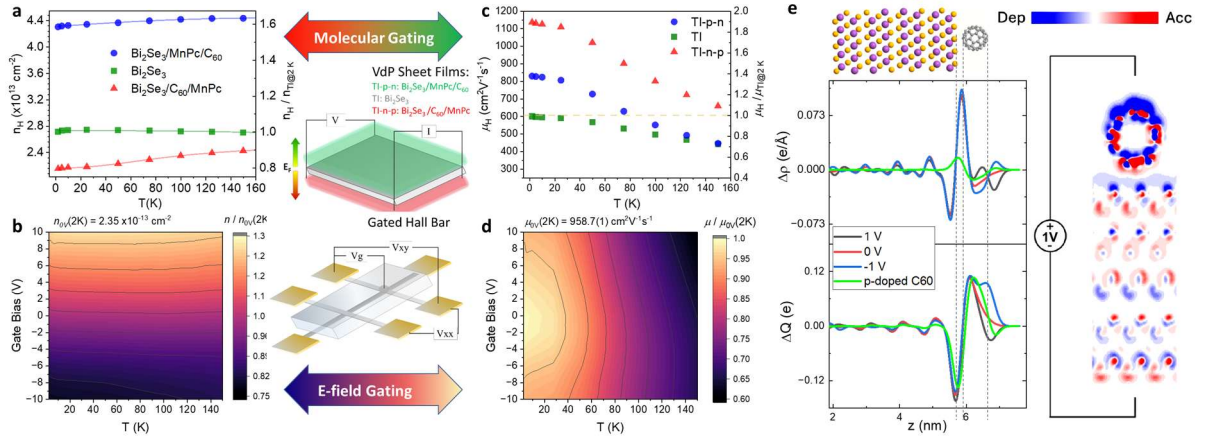


Figure 2 | Molecular gating. Hall effect measurements of **a.** the effect of n - p and p - n molecular diodes on top of a Bi_2Se_3 film 14 nm thick. The n - p bilayer decreases the carrier concentration in the n -type TI, whereas the p - n bilayer increases it. **b.** A similar effect can be achieved with a top-gate requiring a bias of several volts. **c.** The carrier mobility is increased by up to almost factor 2 with the molecular bilayers, probably due to the formation of dispersive bands hybridised with the TI surface states. **d.** The electric bias, independently on the polarity, reduces the carrier mobility at low T . **e.** DFT modelling of the charge and charge density changes at the $\text{Bi}_2\text{Se}_3/\text{C}_{60}$ interface. Top: plane-averaged charge density difference, $\Delta\rho$ (e/Å) vs position. Bottom: integrated charge transfer, $\Delta Q(z) = \int \Delta\rho(z') dz'$. A positive built-in bias of 1 V across the structure or an electron transfer from fullerene to phthalocyanine (4×10^{-3} holes per C atom) are in agreement with observations of carrier concentration and TEM cross-section images.

IV. Weak Anti-localisation and Colossal SOI

X-ray Absorption Spectroscopy (XAS) measurements at the $L_{2,3}$ Se edge show changes in the nonmetal electronic structure with the molecular diode. Whereas the signal at the L_2 edge is enhanced by the molecules, the L_3 region is partly suppressed. The pre L_3 edge at 1435 eV has been associated to hole-charged state of Se in ion-doped Na_xMoSe_2 . [24] This region is enhanced by the $\text{C}_{60}/\text{MnPc}$ (n - p) diode, but not by the $\text{MnPc}/\text{C}_{60}$ (p - n) bilayer, matching the observed changes in carrier concentration from Hall measurements. Magnetic dichroism has been reported in Mn-doped Bi_2Se_3 , [25] but we don't observe any dichroism at the Se edge in either diode configuration, probably due to the lack of interdiffusion and weak coupling of the Mn metal ion in phthalocyanine with the TI substrate (Fig. 3b).

Changes in the spin-dependent scattering of Bi₂Se₃ cannot therefore be attributed to local moments induced by the molecules in the TI film, but rather to changes to the electronic structure and SOI.

Many papers use the expression derived by Hikami et al (HLN) [26] to interpret the magnetoresistance of TI materials. Although this quantum interference (QI) theory has been shown to be valid for Dirac fermions, [27] there are also important differences highlighted in a recent theory [ref] (LHC) that should be taken into account. For example, in both theories the diffusion coefficient is central, $D = \frac{1}{2} v_F^2 \tau$, where τ is the lifetime of a momentum eigenstate. In QI this is normally equated to the elastic lifetime but that is only possible where the spin-orbit lifetime is much less than the elastic lifetime and that is not the case here. In the LHC theory, the diffusion coefficient is a function of the strength of the SOI so we have taken the approach of combining both theories and use the LHC expressions to obtain the diffusion coefficient:

$$D = \frac{v_F^2 \tau_o}{2 + 2\lambda + \frac{5}{4}\lambda^2}$$

Where λ is proportional to the strength of the SOI and is obtained from fitting the MR and τ_o is the elastic lifetime. As we are interested in the SOI lifetime, we use the HLN theory to fit the MR as well, but use the LHC definition for D to obtain the lifetimes.

The full HLN expression describing the correction to the Boltzmann conductance in two dimensions where the magnetic field is perpendicular to the plane of the sample is:

$$\Delta g(B) = -\frac{e^2}{2\pi^2 \hbar} \left[\Psi\left(\frac{1}{2} + \frac{B_1}{B}\right) - \frac{3}{2} \Psi\left(\frac{1}{2} + \frac{B_2}{B}\right) + \frac{1}{2} \Psi\left(\frac{1}{2} + \frac{B_3}{B}\right) \right]$$

Where Ψ is the digamma function and the characteristic fields are:

$$\begin{aligned} B_1 &= B_0 + B_{so} + B_s \\ B_2 &= \frac{4}{3} B_{so} + \frac{2}{3} B_s + B_i \\ B_3 &= 2B_s + B_i \end{aligned}$$

The suffixes stand for potential or elastic (0), inelastic (i), magnetic (s) and spin-orbit (so) scattering. There are four effects accounted for in the HLN equation, magnetic scattering we have ignored since there is no evidence of magnetic impurities in the samples. The elastic scattering rate was determined from the low temperature resistivity and was not treated as a fitting parameter leaving only the inelastic and spin-orbit scattering times. Figure 3c shows the magnetoresistance (MR) for the three different samples measured at 2 K. The positive MR is a signature of strong spin-orbit scattering and is weak antilocalisation. At 2 K, the inelastic phonon scattering has been largely frozen out, so the inelastic scattering is probably due to electron-electron interactions. The fits return nearly the same value of the inelastic time for all samples which is very reassuring. We can then confidently say that the difference in the MR between the samples is due entirely to the SOI.

A value of τ_{SO} of 0.173 ps is indicative of very strong spin-orbit interaction as expected for Bi_2Se_3 . We can compare this τ_{SO} with typical values from disordered metals, for example, amorphous $\text{Cu}_{50}\text{Ti}_{50}$ has a value of 1.0 ps, [28] whereas doping CaAl with Au to increase the SOI produced in $\text{Ca}_{70}\text{Al}_{28}\text{Au}_2$ a value of 0.14 ps. [29,30] The samples with $\text{C}_{60}/\text{MnPc}$ and $\text{MnPc}/\text{C}_{60}$ have increased the spin-orbit interaction to values of 0.107 ps and 0.085 ps, which is remarkable and comparable to that found in e.g. in $\text{Pd}_{80}\text{Si}_{20}$ of 0.09 ps. [31] Since the TI material in all samples is the same, we can estimate (using \hbar/τ_{SO}) that the addition of a layer of $\text{C}_{60}/\text{MnPc}$ has increased the SOI energy by 2.5 meV and the $\text{MnPc}/\text{C}_{60}$ layer by 4.2 meV -both with the same sign and despite the opposite change in carrier density.

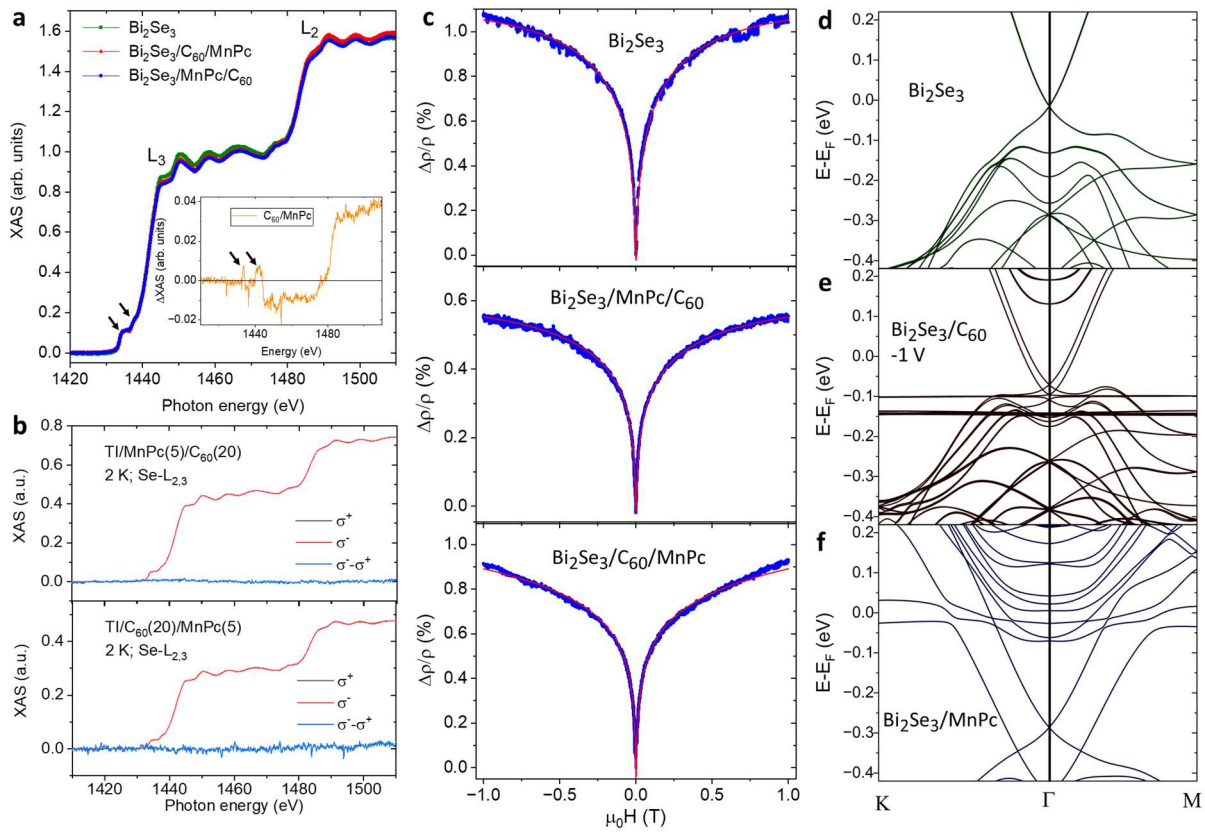


Figure 3| SOI and electronic structure in molecular gated Bi_2Se_3 . **a.** X-ray Absorption Spectroscopy (XAS) at Se $L_{2,3}$ edge for Bi_2Se_3 pristine and with molecular diodes on top. **b.** X-ray Magnetic Circular Dichroism at the Se $L_{2,3}$ edge with molecular diodes shows no magnetic order. **c.** Measurements of weak anti-localisation and fit to the HNL model for Bi_2Se_3 pristine (top), with a p-n (middle) and an n-p molecular diode overlayer (bottom). Parameters derived from the fit are in Table 1. DFT simulations of the band structure in **d.** pristine, **e.** with a C_{60} interface in which the diode is modelled as a negative voltage and **f.** for $\text{Bi}_2\text{Se}_3/\text{MnPc}$. The molecular gating leads to the formation of flat bands near the Fermi level, which can result in strongly correlated effects, enhanced SOI and Berry curvature.

Figs. 3d-f illustrate the electronic band structure evolution along K - Γ - M high-symmetry points for 5 quintuple layers (5QL) pristine Bi_2Se_3 , $\text{Bi}_2\text{Se}_3(5\text{QL})/\text{C}_{60}$ and $\text{Bi}_2\text{Se}_3(5\text{QL})/\text{C}_{60}$ with a molecular bias. The pristine Bi_2Se_3 shows a well-defined gapless Dirac cone at the Γ -point, characteristic of topological surface states. The bands exhibit a smooth dispersion, confirming the unperturbed topological nature of the system. Adding a C_{60} interface leads to hybridisation near the Dirac point and the emergence of flat bands near the Fermi level, originating from the molecular orbitals. These bands may be partly localised, contributing to an enhanced Berry curvature, [32,33] as observed in topological systems such as twisted graphene and bilayer Kagome metals. [34–37] Taking into consideration the differences in band gaps (1.2 eV in MnPc vs 2.3 eV in C_{60}) and associated shift in the HOMO and LUMO levels at the molecular interface, [38] a 1 V built-in bias makes the flat bands much more pronounced, indicating stronger localisation of electronic states. The shift of these states further from the Dirac cone suggests enhanced charge transfer, as observed experimentally when comparing a TI/ C_{60} interface with TI/ C_{60} /MnPc (Supplementary table), and a greater molecular orbital contribution in the electronic structure that results in the stronger SOI.

Table 1: Carrier parameters of pristine and molecular-gated Bi_2Se_3 .

Parameter @2K	TI	TI/n-p	TI/p-n
$\rho_0[\mu\Omega\text{cm}]$	517 ± 3	358 ± 2	249 ± 1
$n_H[10^{13} \text{ cm}^{-2}]$	2.708 ± 0.003	2.152 ± 0.002	4.298 ± 0.004
$\mu[\text{cm}^2\text{V}^{-1}\text{s}^{-1}]$	601.0 ± 0.8	1136 ± 2	829 ± 1
$D[\text{cm}^2/\text{s}]$	58.8 ± 0.2	102.2 ± 0.1	112.2 ± 0.1
$\tau_{\text{SO}}[10^{-12} \text{ s}]$	0.173 ± 0.002	0.107 ± 0.002	0.085 ± 0.001
$l_{\text{SO}} [\text{nm}]$	32	33	31
$\tau_i[10^{-12}\text{s}]$	33.5 ± 0.3	32.2 ± 0.3	21.5 ± 0.4
$\tau_0[10^{-12}\text{s}]$	$0.044 \pm .006$	0.078 ± 0.001	0.057 ± 0.002
m.f.p. [nm]	$32.77 \pm .04$	57.56 ± 0.08	52.92 ± 0.08
$\Theta_D[\text{K}]$	$271.4 \pm .2$	265.1 ± 0.2	$237.9 \pm .2$

V. Vibrational Modes and Optical Tuning

The spin-orbit interaction results in a slow-down of the three main vibrational modes in Bi_2Se_3 ; the out-of-plane modes A_{1g}^1 and A_{1g}^2 (Raman shifts of 73 and 175 cm^{-1}) and the in-plane mode E_g^2 (133 cm^{-1}), see Fig. 4a. [39–42] In our measurements, Bi_2Se_3 wafers partly covered by molecular diodes and probed with a low energy red laser (633 nm) show a slower oscillation frequency for all three modes in both n-p and p-n covered areas, but the effect is stronger for MnPc/ C_{60} (n-p) in the A_{1g}^2 mode, see Fig. 4b. A softening of the vibrational modes is consistent with a stronger SOI, [43] and may also be linked with changes in the Debye temperature observed in Bloch-Gruneissen fits of the resistivity vs. temperature, see Table 1 and Supplementary Fig. S1. Significantly, this slowdown is a function of the excitation wavelength, with a blue-shift of the vibrational modes in Bi_2Se_3 /diode samples w.r.t. to pristine Bi_2Se_3 as the photon energy increases. The reduced or even inverted effect at higher photon

energies may be due to exciton generation across the HOMO-LUMO energy gaps in C₆₀ and phthalocyanine (~2.3 and 1.6 eV), leading to a reduced charge transfer and decoupling of the molecular/TI interface.

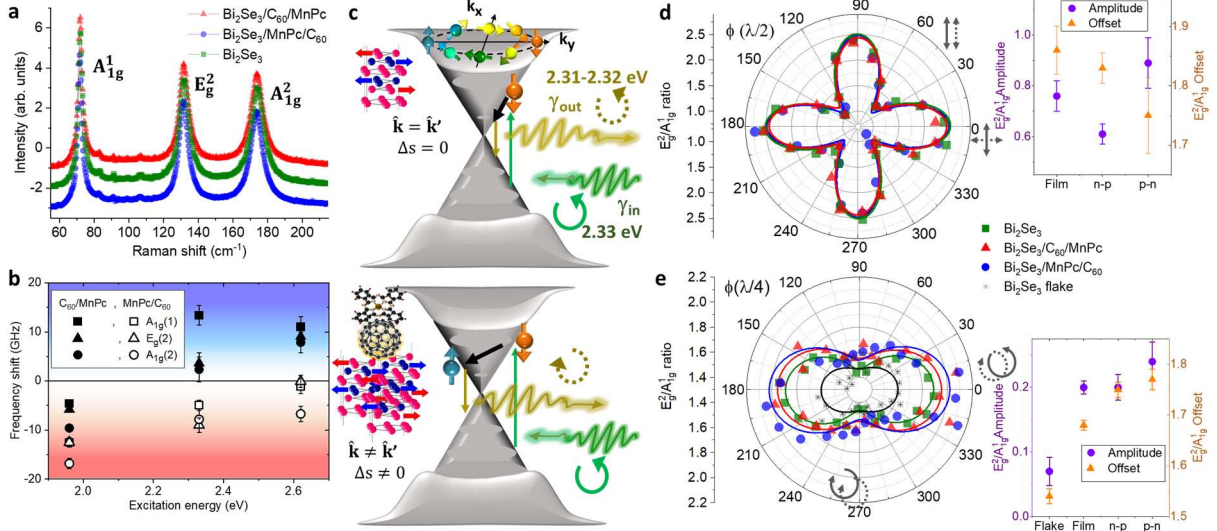


Figure 4| Raman spectroscopy and optical gating of the SOI. **a.** Raman spectra of Bi₂Se₃ with and without molecular bilayers. **b.** The Raman modes are slowed/softened by the molecular diodes. This effect can be cancelled by light exposure above the HOMO-LUMO gap (~2.3 eV). Spectra are averaged over 24 sample points. **c.** Schematic of circularly polarised Raman spectroscopy of the E_g² (in-plane) vibration. An electron excited from the valence to the conduction band by 532 nm circularly polarised light (2.33 eV) will conserve its spin during the excitation and decay. Some of the energy is transferred to a vibration (~0.02 eV for the 135 cm⁻¹ mode). SOI and lattice scattering can flip the electron spin and result in the emission of a photon with opposite polarisation. **d.** Comparison of the E_g to A_{1g}² intensities with incident linearly polarised light rotated from parallel (Y) to perpendicular (X) to the detector (Y) with a λ/2 waveplate (φ polariser angle). **e.** Ratio of in-plane (E_g²) to out-of-plane (A_{1g}²) Raman mode scattering intensity with a left-handed circularly polarised detector as the incident polarisation is changed between right-handed and left-handed with a λ/4 plate. Lines in e and f are fits to a cos (2φ and φ) function. Insets in d. and e. are the fit parameters.

Polarised Raman spectroscopy may also offer a means to probe the spin-orbit interaction and surface states in Bi₂Se₃. Due to crystal symmetry, the A_{1g} modes are quenched when measuring with cross-polarised linear light (e.g. excitation in X and probing in Y), and maximised when the polarisation of the excitation and probe are parallel (XX or YY). [44,45] This is the case in all our samples, independently of the coverage of the TI film (Fig. 4d). Molecular gating therefore has no influence on the symmetry of in-plane and out-of-plane vibrations as probed by linearly polarised light. The situation changes when probing the system with circularly polarized light (Fig. 4e). Also for symmetry considerations, measuring in a cross-polarisation setup (e.g. right-handed circular excitation and left-

handed circular probing or RL) leads to maximum intensity in the out-of-plane mode E_g and minimum intensity for the in-plane modes (A_{2g}^1, A_{2g}^2). [46] When the polarisation handedness is conserved between excitation and probing, e.g. RR, the opposite situation takes place, with a minimum out of plane E_g mode intensity. The situation can be enhanced by spin-orbit coupling during resonant Raman scattering, i.e. when electrons may be promoted from the valence to the conduction band. Due to spin conservation during optical absorption ($\Delta S = 0$), excitation with e.g. left-handed circular polarised light will promote spin-up electrons to a higher energy state. During Raman scattering, some of the electron momentum is transferred to a vibrational mode and the electron will lose energy before decaying back to the lower energy state. Due to spin-momentum locking at the surface of the TI, the emitted photon will only have the same polarisation as the absorbed one only if the electron conserves its momentum direction ($\hat{\mathbf{k}} = \hat{\mathbf{k}}'$). A change of the momentum direction in the XY plane ($\hat{\mathbf{k}} \neq \hat{\mathbf{k}}'$) must be accompanied by spin transfer to the lattice via the SOI and the emission of a photon with a different polarisation. This can happen if the SOI is strong and τ_{so} is of the same order as the lifetime of the virtual state, typically $\sim 10^{-13}$ - 10^{-14} s. [47,48] The cross-polarised emission at the E_g peak will therefore be larger for thin film Bi_2Se_3 compared to quasi-bulk crystals (flakes). In Bi_2Se_3 film regions covered by a molecular diode, we can observe that the very short spin-orbit time results in further enhancement of this cross-polarised in-plane mode emission in the RL (or LR) configuration.

Conclusions

Molecular diodes offer an alternative to gating the electronic states of TI thin films and 2-dimensional materials. This ‘gentle’ method leads to a tuning in the carrier density and enhanced mobility. Surprisingly, it also results in a strong enhancement of what was already a very strong SOI, with scattering fields and spin-orbit magnetic fields that are significantly larger than reported values. The strengthened spin-orbit interaction can lead to new physics, with tight Berry curvatures and polarised vibrational coupling. This dependence on excitation energy allows for the optical gating of the vibrational frequency.

METHODS

Deposition: TI-Molecule hybrid thin films were fabricated using a multi-chamber deposition system allowing ultra-high vacuum (10^{-10} mbar) transfer of wafers between individual molecular beam epitaxy reactors. [0001] oriented Al_2O_3 wafers with dimensions 20 mm x 20 mm were precleaned in acetone and isopropanol alcohol before being outgassed at 500 °C in the UHV chamber before growth. The Bi_2Se_3 layer was co-evaporated with a Bi:Se flux ratio of 1:40 while maintaining the substrate temperature at 235 °C. After growing 14 nm at 0.15 nm/min the epitaxial material is cooled to 150 °C in a selenium only flux to limit the creation of Se vacancies. Detailed characterisation and methodology

for these TI films can be found in previous works. [49] The TI film is then transferred under UHV to separate chamber where the single wafer is masked to create the three unique films. The commercially available MnPc and C₆₀ powders were evaporated from low-temperature Knudsen cells at 430 and 500 °C respectively. During the molecule evaporation the substrate was maintained at an ambient temperature, once again, to limit the risk of Se vacancy generation.

Transport: Transport measurements were taken on separated diced 4mm x 4mm wafers of the plain and molecular coated TI films using a Van der Pauw geometry for characterising the Hall coefficients and sheet resistance as a function of measurement temperature. Such organic films are incompatible with traditional fabrication processed to their high solubility. Separate plain films grown with nominally the same process were processed into Hall bars with a 24 nm Alumina gate dielectric grown by ALD to compare the effect of purely E-field gating upon the magneto-transport.

NEXAFS/XMCD: Measurements at the BOREAS beamline of the ALBA Synchrotron.

Raman: Raman spectroscopy was carried out with a Horiba LabRam HR800 instrument using blue (473 nm), green (532 nm) and red (633 nm) laser excitation, and with an 1800 ln/mm grating. Linearly polarised measurements were carried out with red and blue excitation, and circularly polarised measurements with green. Linear polarisers, lambda quarter and lamda half plates were used in the measurements to rotate the excitation and probing polarisations. Peak positions were obtained with red light excitation measuring in 32 different sample points and averaging the final result.

DFT: First-principles calculations were conducted using density functional theory (DFT) as implemented in QuantumATK. [50] The calculations employed a linear combination of numerical atomic orbitals (LCAO) basis set within the generalized gradient approximation (GGA) framework, using norm-conserving pseudopotentials sourced from PseudoDojo. [51] To accurately capture the Dirac cone surface states in the 2D energy-momentum relationship, spin-orbit coupling (SOC) was incorporated via fully relativistic pseudopotentials. Brillouin-zone integrations were performed using a k-point grid generated via the Monkhorst-Pack scheme, [52] with a density of approximately 10 k-points per Å. A plane-wave energy cutoff of 125 Ha was used for the discretised grid, and all structural relaxations were carried out until the maximum force on any atom was below 0.02 eV/Å. To account for inter- and intra-molecular noncovalent interactions, van der Waals (vdW) corrections were applied to the GGA functional. [53] The slab model in the supercell was designed to be infinite and periodic in the x- and y-directions (parallel to the slab surface) but finite along the z-direction (normal to the slab). To eliminate spurious interactions between neighbouring periodic images, a vacuum region exceeding 20 Å was added along the z-direction. In slab calculations with asymmetric surfaces, periodic boundary conditions can introduce an artificial macroscopic electrostatic field. [54] To mitigate this, mixed

Neumann and Dirichlet boundary conditions were applied at the C_{60} and Bi_2Se_3 sides of the slab, respectively, serving as an alternative approach for dipole correction. [55] The absence of an artificial electrostatic field at zero applied field was verified by analysing the planar-averaged Hartree potential, where a flat vacuum potential profile confirmed the effectiveness of the correction.

TEM: Electron transparent lamella of the samples were prepared by focused ion beam (FIB) lift-out techniques using a dual beam electron-beam/FIB instrument, a Thermo Fisher Helios Xe Plasma FIB. A 30 kV xenon beam was used to mill into the bulk with currents 6.7 nA and 1.8 nA to extract a section which was subsequently thinned using a current of 74 pA and polished with a 5 kV 47pA ion beam to a minimum thickness of between 55 - 75 nm. STEM and EFTEM imaging was performed in a JEOL ARM200cF at 80 kV.

ACKNOWLEDGEMENTS

We thank the Engineering and Physical Sciences Research Council UK for support via grants EP/S030263/1 and EP/X027074/1. OC and HV acknowledge the support of the EC project INTERFAST (H2020-FET-OPEN-965046). We also acknowledge the support of the Henry Royce Institute for Advanced Materials for access to the Royce Deposition System facilities at the University of Leeds; EPSRC Grant Number EP/P022464/1. T.M. thanks the Royal Society of Engineering for support via the fellowship RF\201920\19\245.

- [1] N. H. D. Khang, Y. Ueda, and P. N. Hai, A conductive topological insulator with large spin Hall effect for ultralow power spin-orbit torque switching, *Nat Mater* **17**, 808 (2018).
- [2] E. Derunova, Y. Sun, C. Felser, S. S. P. Parkin, B. Yan, and M. N. Ali, Giant intrinsic spin Hall effect in W_3Ta and other A15 superconductors, *Sci Adv* **5**, (2019).
- [3] D. C. Mahendra et al., Room-temperature high spin-orbit torque due to quantum confinement in sputtered $Bi_xSe_{(1-x)}$ films, *Nat Mater* **17**, 800 (2018).
- [4] J. H. Han, A. Richardella, S. A. Siddiqui, J. Finley, N. Samarth, and L. Q. Liu, Room-Temperature Spin-Orbit Torque Switching Induced by a Topological Insulator, *Phys Rev Lett* **119**, (2017).
- [5] Y. Lv, J. Kally, D. L. Zhang, J. S. Lee, M. Jamali, N. Samarth, and J. P. Wang, Unidirectional spin-Hall and Rashba-Edelstein magnetoresistance in topological insulator-ferromagnet layer heterostructures, *Nat Commun* **9**, (2018).
- [6] M. Jamali, J. S. Lee, J. S. Jeong, F. Mahfouzi, Y. Lv, Z. Y. Zhao, B. K. Nikolic, K. A. Mkhoyan, N. Samarth, and J. P. Wang, Giant Spin Pumping and Inverse Spin Hall Effect in the Presence of Surface and Bulk Spin-Orbit Coupling of Topological Insulator Bi_2Se_3 , *Nano Lett* **15**, 7126 (2015).

- [7] J. L. Yu, X. L. Zeng, L. G. Zhang, K. He, S. Y. Cheng, Y. F. Lai, W. Huang, Y. H. Chen, C. M. Yin, and Q. K. Xue, Photoinduced Inverse Spin Hall Effect of Surface States in the Topological Insulator Bi_2Se_3 , *Nano Lett* **17**, 7878 (2017).
- [8] J. L. Yu, X. L. Zeng, L. G. Zhang, C. M. Yin, Y. H. Chen, Y. Liu, S. Y. Cheng, Y. F. Lai, K. He, and Q. K. Xue, Inverse spin Hall effect induced by linearly polarized light in the topological insulator Bi_2Se_3 , *Opt Express* **26**, 4832 (2018).
- [9] T. Moorsom et al., Reversible spin storage in metal oxide-fullerene heterojunctions, *Sci Adv* **6**, (2020).
- [10] P. Sessi, T. Bathon, K. A. Kokh, O. E. Tereshchenko, and M. Bode, Probing the Electronic Properties of Individual MnPc Molecules Coupled to Topological States, *Nano Lett* **14**, 5092 (2014).
- [11] Y. R. Song, Y. Y. Zhang, F. Yang, K. F. Zhang, C. Liu, D. Qian, C. L. Gao, S. B. Zhang, and J. F. Jia, Magnetic anisotropy of van der Waals absorbed iron(II) phthalocyanine layer on Bi_2Te_3 , *Phys Rev B* **90**, (2014).
- [12] D. W. Latzke, C. Ojeda-Aristizabal, S. M. Griffin, J. D. Denlinger, J. B. Neaton, A. Zettl, and A. Lanzara, Observation of highly dispersive bands in pure thin film C_{60} , *Phys Rev B* **99**, (2019).
- [13] L. Wu, R. M. Ireland, M. Salehi, B. Cheng, N. Koirala, S. Oh, H. E. Katz, and N. P. Armitage, Tuning and stabilizing topological insulator Bi_2Se_3 in the intrinsic regime by charge extraction with organic overlayers, *Appl Phys Lett* **108**, (2016).
- [14] F. Al Ma'Mari et al., Beating the Stoner criterion using molecular interfaces, *Nature* **524**, 69 (2015).
- [15] F. Al Ma'Mari et al., Emergent magnetism at transition-metal-nanocarbon interfaces, *Proc Natl Acad Sci U S A* **114**, 5583 (2017).
- [16] T. Moorsom et al., Spin-polarized electron transfer in ferromagnet/ C_{60} interfaces, *Phys Rev B* **90**, (2014).
- [17] S. Alotibi et al., Enhanced Spin-Orbit Coupling in Heavy Metals via Molecular Coupling, *ACS Appl Mater Interfaces* **13**, 5228 (2021).
- [18] E. Lesne et al., Designing spin and orbital sources of Berry curvature at oxide interfaces, *Nat Mater* **22**, 576 (2023).
- [19] Y. Cao, D. Chowdhury, D. Rodan-Legrain, O. Rubies-Bigorda, K. Watanabe, T. Taniguchi, T. Senthil, and P. Jarillo-Herrero, Strange Metal in Magic-Angle Graphene with near Planckian Dissipation, *Phys Rev Lett* **124**, (2020).
- [20] A. Ghiotto et al., Quantum criticality in twisted transition metal dichalcogenides, *Nature* **597**, 345 (2021).
- [21] S. Javaid and M. J. Akhtar, Orientation dependant charge transfer at fullerene/Zn-phthalocyanine ($\text{C}_{60}/\text{ZnPc}$) interface: Implications for energy level alignment and photovoltaic properties, *Appl Phys Lett* **109**, (2016).

- [22] A. L. Ayzner, D. Nordlund, D. H. Kim, Z. N. Bao, and M. F. Toney, Ultrafast Electron Transfer at Organic Semiconductor Interfaces: Importance of Molecular Orientation, *Journal of Physical Chemistry Letters* **6**, 6 (2015).
- [23] N. Sai, R. Gearba, A. Dolocan, J. R. Tritsch, W. L. Chan, J. R. Chelikowsky, K. Leung, and X. Y. Zhu, Understanding the Interface Dipole of Copper Phthalocyanine (CuPc)/C60: Theory and Experiment, *Journal of Physical Chemistry Letters* **3**, 2173 (2012).
- [24] A. Plewa, A. Kulka, E. Hanc, J. G. Sun, M. Nowak, K. Redel, L. Lu, and J. Molenda, Abnormal Phenomena of Multi-Way Sodium Storage in Selenide Electrode, *Adv Funct Mater* **31**, (2021).
- [25] L. J. Collins-McIntyre et al., X-ray magnetic spectroscopy of MBE-grown Mn-doped Bi₂Se₃ thin films, *AIP Adv* **4**, (2014).
- [26] S. Hikami, A. I. Larkin, and Y. Nagaoka, SPIN-ORBIT INTERACTION AND MAGNETORESISTANCE IN THE 2 DIMENSIONAL RANDOM SYSTEM, *Progress of Theoretical Physics* **63**, 707 (1980).
- [27] E. McCann, K. Kechedzhi, V. I. Fal'ko, H. Suzuura, T. Ando, and B. L. Altshuler, Weak-localization magnetoresistance and valley symmetry in graphene, *Phys Rev Lett* **97**, (2006).
- [28] B. J. Hickey, D. Greig, and M. A. Howson, SPIN ORBIT SCATTERING IN AMORPHOUS CUTI ALLOYS, *Journal of Physics F-Metal Physics* **16**, L13 (1986).
- [29] A. Sahnoune, J. O. Stromolsen, and H. E. Fischer, INFLUENCE OF SPIN-ORBIT SCATTERING ON THE MAGNETORESISTANCE DUE TO ENHANCED ELECTRON-ELECTRON INTERACTIONS, *Phys Rev B* **46**, 10035 (1992).
- [30] A. Sahnoune, J. O. Stromolsen, and A. Zaluska, QUANTUM CORRECTIONS TO THE CONDUCTIVITY IN ICOSAHEDRAL AL-CU-FE ALLOYS, *Phys Rev B* **46**, 10629 (1992).
- [31] J. B. Bieri, A. Fert, G. Creuzet, and A. Schuhl, WEAK LOCALIZATION IN METALLIC GLASSES .1. MAGNETORESISTANCE, *Journal of Physics F-Metal Physics* **16**, 2099 (1986).
- [32] D. Varjas, A. Abouelkomsan, K. Yang, and E. J. Bergholtz, Topological lattice models with constant Berry curvature, *Scipost Physics* **12**, (2022).
- [33] L. Chen, T. Mazaheri, A. Seidel, and X. Tang, The impossibility of exactly flat non-trivial Chern bands in strictly local periodic tight binding models, *Journal of Physics A-Mathematical and Theoretical* **47**, (2014).
- [34] E. J. Bergholtz and Z. Liu, TOPOLOGICAL FLAT BAND MODELS AND FRACTIONAL CHERN INSULATORS, *Int J Mod Phys B* **27**, (2013).
- [35] T. Devakul, V. Crépel, Y. Zhang, and L. Fu, Magic in twisted transition metal dichalcogenide bilayers, *Nat Commun* **12**, (2021).
- [36] J. X. Yin et al., Negative flat band magnetism in a spin-orbit-coupled correlated kagome magnet, *Nat Phys* **15**, 443 (2019).
- [37] J. X. Hu, Y. M. Xie, and K. T. Law, Berry curvature, spin Hall effect, and nonlinear optical response in moire transition metal dichalcogenide heterobilayers, *Phys Rev B* **107**, (2023).
- [38] D. Waas, F. Rücker, M. Knupfer, and B. Büchner, Energy-level alignment at interfaces between manganese phthalocyanine and C₆₀, *Beilstein Journal of Nanotechnology* **8**, 927 (2017).

- [39] K. M. F. Shahil, M. Z. Hossain, V. Goyal, and A. A. Balandin, Micro-Raman spectroscopy of mechanically exfoliated few-quintuple layers of Bi_2Te_3 , Bi_2Se_3 , and Sb_2Te_3 materials, *J Appl Phys* **111**, (2012).
- [40] G. H. Zhang, H. J. Qin, J. Teng, J. D. Guo, Q. L. Guo, X. Dai, Z. Fang, and K. H. Wu, Quintuple-layer epitaxy of thin films of topological insulator Bi_2Se_3 , *Appl Phys Lett* **95**, (2009).
- [41] W. Richter, H. Kohler, and C. R. Becker, RAMAN AND FAR-INFRARED INVESTIGATION OF PHONONS IN RHOMBOHEDRAL V2-VI3 COMPOUNDS - Bi_2Te_3 , Bi_2Se_3 , Sb_2Te_3 AND $\text{Bi}_2(\text{Te}_{1-x}\text{Se}_x)_3$ (0 LESS THAN X LESS THAN 1), $(\text{Bi}_{1-y}\text{Sb}_y)_2\text{Te}_3$ (0 LESS THAN Y LESS THAN 1), *Physica Status Solidi B-Basic Research* **84**, 619 (1977).
- [42] J. Zhang, Z. P. Peng, A. Soni, Y. Y. Zhao, Y. Xiong, B. Peng, J. B. Wang, M. S. Dresselhaus, and Q. H. Xiong, Raman Spectroscopy of Few-Quintuple Layer Topological Insulator Bi_2Se_3 Nanoplatelets, *Nano Lett* **11**, 2407 (2011).
- [43] B. T. Wang and P. Zhang, Phonon spectrum and bonding properties of Bi_2Se_3 : Role of strong spin-orbit interaction, *Appl Phys Lett* **100**, (2012).
- [44] H. H. Kung et al., Surface vibrational modes of the topological insulator Bi_2Se_3 observed by Raman spectroscopy, *Phys Rev B* **95**, (2017).
- [45] B. Irfan, S. Sahoo, A. P. S. Gaur, M. Ahmadi, M. J. F. Guinel, R. S. Katiyar, and R. Chatterjee, Temperature dependent Raman scattering studies of three dimensional topological insulators Bi_2Se_3 , *J Appl Phys* **115**, (2014).
- [46] V. Gnezdilov, Y. G. Pashkevich, H. Berger, E. Pomjakushina, K. Conder, and P. Lemmens, Helical fluctuations in the Raman response of the topological insulator Bi_2Se_3 , *Phys Rev B* **84**, (2011).
- [47] L. Wei and W. Min, Electronic Preresonance Stimulated Raman Scattering Microscopy, *Journal of Physical Chemistry Letters* **9**, 4294 (2018).
- [48] G. Dall'Osto and S. Corni, Time Resolved Raman Scattering of Molecules: A Quantum Mechanics Approach with Stochastic Schroedinger Equation, *Journal of Physical Chemistry A* **126**, 8088 (2022).
- [49] V. Pistore et al., Terahertz Plasmon Polaritons in Large Area Bi_2Se_3 Topological Insulators, *Adv Opt Mater* **12**, (2024).
- [50] S. Smidstrup et al., QuantumATK: an integrated platform of electronic and atomic-scale modelling tools, *Journal of Physics-Condensed Matter* **32**, (2020).
- [51] M. J. van Setten, M. Giantomassi, E. Bousquet, M. J. Verstraete, D. R. Hamann, X. Gonze, and G. M. Rignanese, The PSEUDODOJO: Training and grading a 85 element optimized norm-conserving pseudopotential table, *Comput Phys Commun* **226**, 39 (2018).
- [52] H. J. Monkhorst and J. D. Pack, SPECIAL POINTS FOR BRILLOUIN-ZONE INTEGRATIONS, *Phys Rev B* **13**, 5188 (1976).
- [53] S. Grimme, J. Antony, S. Ehrlich, and H. Krieg, A consistent and accurate ab initio parametrization of density functional dispersion correction (DFT-D) for the 94 elements H-Pu, *Journal of Chemical Physics* **132**, (2010).

- [54] J. Neugebauer and M. Scheffler, ADSORBATE-SUBSTRATE AND ADSORBATE-ADSORBATE INTERACTIONS OF NA AND K ADLAYERS ON AL(111), Phys Rev B **46**, 16067 (1992).
- [55] G. Makov and M. C. Payne, PERIODIC BOUNDARY-CONDITIONS IN AB-INITIO CALCULATIONS, Phys Rev B **51**, 4014 (1995).